Acta Biomaterialia xxx (xxxx) xxx

Contents lists available at ScienceDirect

Acta Biomaterialia

journal homepage: www.elsevier.com/locate/actbio

Full length article

Digital light processing programs shape-morphing hydrogels into undulating 3D scaffolds supporting corneal limbal epithelial organization

Ioannis Paschalidis [a,b,c], François Chatelain [b,c], Remy Agniel [d], Christophe Sandt [e], Damien Guindolet [a,b], Sabrina Kellouche [d], Alexandra Fuchs [b,c], Benoit Souquet [a,b,1,*], Eric Ernest Gabison [a,b,1,*]

[a] Translational Research and Experimental Corneal Surgery (TREX), Hôpital Fondation A. de Rothschild, Paris, France
[b] Université Paris Cité, Inserm, IRSL Institut de Recherche Saint Louis, U1342, Paris, France
[c] CEA IRIG, Grenoble, France
[d] Equipe de Recherche sur les Relations Matrice Extracellulaire Cellules, ERRMECe (EA1391), Institut des Matériaux, I-MAT (FD4122), CY Cergy Paris Université, Cergy Pontoise, France
[e] SMIS beamline, Synchrotron SOLEIL, Saint Aubin, France

ARTICLE INFO

Keywords:
Cornea
Digital light processing bioprinting
Silk fibroin
Limbal epithelial stem cells
Shape morphing hydrogel

ABSTRACT

The cornea serves as a transparent protective barrier for the eye, with epithelial homeostasis and renewal critically dependent on limbal epithelial stem cells residing in a specialized niche characterized by stromal invaginations that form limbal crypts. Elegant advanced *in vitro* models of the limbal niche have been described, but most are technologically demanding, requiring multi-step fabrication that limits scalability. We developed a simple and rapid strategy to fabricate 3D scaffolds with undulating topography using a shape-morphing hydrogel concept. A photocrosslinkable bioink composed of methacrylated collagen, hyaluronic acid, and silk fibroin was patterned using grayscale UV projection. Digital Light Processing technology enabled spatially controlled heterogeneous crosslinking densities in a single-step process. The undulating topography was then formed through differential shrinking dynamics of the hydrogel at 37 °C; specifically, the volume of areas exposed to lower UV doses decreased while areas exposed to higher UV doses remained stable. The addition of silk fibroin proved essential for both temperature-dependent shape morphing and sustained corneal epithelial cell adhesion and growth. The undulating scaffolds supported epithelial stratification for at least three weeks in culture. Physiologically relevant corneal mechanotransduction and apicobasal organization was achieved, with nuclear YAP localization in soft areas, P63-positive progenitor cells enriched in basal layers and PAX6-positive differentiated cells in apical layers. Additionally, progressive epithelial maturation was demonstrated by increased CK3 expression, establishment of tight junctions, and the deposition of a basement membrane.

Statement of significance: Paschalidis *et al.* This work offers dual significance. First, we introduce an innovative, simple and single-step bioprinting approach to create 3D scaffolds with complex topography. Using Digital Light Processing technology, a silk fibroin-containing photocurable bioink is exposed to spatially heterogeneous UV doses. This enables differential crosslinking densities in the printed scaffold, which undergoes programmable shape-morphing. Second, we applied this methodology to engineer advanced corneal models that recapitulate the structural features of the epithelial stem cell niche, an undulating topography. This addresses critical needs in human disease modeling and preclinical testing while reducing animal use. The resulting model sustains three-week cultures and faithfully mimics physiological epithelial organization, with progenitor markers expressed in basal layers and differentiation markers indicating barrier function in apical layers.

* Corresponding authors at: Translational Research and Experimental Corneal Surgery (TREX), Hôpital Fondation A. de Rothschild, Paris, France.
E-mail addresses: bsouquet@for.paris (B. Souquet), egabison@for.paris (E.E. Gabison).
[1] These authors contributed equally to this work.

https://doi.org/10.1016/j.actbio.2026.06.002
Received 4 February 2026; Accepted 1 June 2026
Available online 3 June 2026

1. Introduction

Advanced *in vitro* models, microphysiological systems and organoids on a chip have gained increasing attention over the past decade. The convergence of tissue engineering, stem cell biology and regulatory demands has underscored the need for human-relevant and ethically acceptable experimental platforms. These models are designed to provide controlled environments that guide self-assembly of tissue-like structures with physiological and/or pathological relevance, enabling the study of complex biological processes with a high degree of reproducibility and tunability [1–3]. Beyond fundamental research, such platforms carry direct translational relevance, for instance, in the preclinical development of Advanced Therapy Medicinal Products (ATMPs) targeting corneal pathologies such as Aniridia-Associated limbal stem cell deficiency [4]. In this context, human biomimetic limbal niche models offer a scalable and ethically advantageous alternative to animal models, particularly for assessing the functionality, the potency, epithelial penetration, and biological activity of novel therapeutics such as engineered extracellular vesicles, parameters that are inherently difficult to evaluate in species-mismatched murine systems or classical cell culture systems.

In the case of the cornea, several strategies have been explored to engineer corneal curvature [5–7] and limbal structures [8–11] with varying degrees of biomimicry. The limbus is a circumferential transition zone between the cornea and conjunctiva. It is characterized by radially oriented ridges known as the palisades of Vogt and associated stromal invaginations that form limbal crypts, which constitute the niche for limbal epithelial stem cells (LESCs) [12]. Early studies using collagen hydrogel molding demonstrated that engineered limbal crypt-like geometries promoted stratification of P63-positive epithelial progenitors along these biomimetic niches [9]. Subsequent work employing microstereolithography of polyethylene glycol diacrylate (PEGDA) generated ring-shaped constructs with micropockets mimicking limbal crypts, enhancing epithelial migration and proliferation [8]. More recently, two-photon polymerization of gelatin methacryloyl (GelMA) was used to reproduce complex limbal topographies, inducing spatial zonation of proliferative and differentiating epithelial phenotypes along 3D gradients [10]. Collectively, these studies have demonstrated that bioengineering approaches enable the fabrication of advanced *in vitro* corneal limbal models with physiological relevance in regulating epithelial stemness, migration, regeneration, and differentiation.

Despite these significant advances, most existing models remain technologically demanding, relying on multi-step fabrication processes and low-throughput workflows that limit scalability. Additionally, sustaining epithelial cultures over extended periods remains challenging across platforms, especially when seeking to maintain both mature and immature epithelial cells on a self-organized basement membrane (BM). As a result, translation into routine laboratory use, screening or toxicological platforms remain limited.

Our goal was to develop a model that preserves the essential biomimetic and functional properties of previous systems while reducing technological complexity, fabrication time, and cost. To this end, we aimed for a one-step, versatile, tunable and scalable process capable of generating 3D architectures conducive to epithelial cell attachment, stratification, and differentiation. We employed Digital Light Processing (DLP), a high-resolution photocuring technology that we had previously applied to biliary and vascular tissue engineering [13,14] and here adapted for corneolimbal applications.

By applying smart design to create heterogeneous crosslinking densities within a smart material (a photocurable composite bioink composed of methacrylated silk fibroin, collagen type I, and hyaluronic acid), we fabricated undulating scaffolds in a single step. These scaffolds reproduced key topographical features of the limbal niche in a scalable and reproducible manner.

In this study, we first identify an optimal bioink composition that ensures scaffold stability and printability while supporting cell growth. We then investigate how crosslinking density regulates cellular mechanotransduction, in line with published data on YAP signaling in corneal epithelial cells [15]. Additionally, we analyze how shape-morphing induced surface topography leads to the formation of wavy hydrogels promoting corneal epithelial cell stratification. We have successfully demonstrated that this system supports limbal epithelial cell culture for up to three weeks, exhibiting an apicobasal organization indicative of epithelial differentiation.

2. Materials and methods

2.1. Hydrogel solution preparation

Three different natural polymers modified with methacryloyl groups (MA), along with the photoinitiator (LAP), were used in this project (Table 1). All components were provided as sterile products by the manufacturer. LAP, HAMA and SFMA were resuspended from their freeze-dried form in 1x PBS under sterile conditions in a laminar flow hood. Collagen I methacrylate (ColMA) was resuspended in (20 mM) acetic acid at 4 °C overnight. Before use, ColMA was neutralized with a solution provided by the manufacturer. The final bioink was prepared just before printing by sequentially mixing all components. All solutions were kept on ice, to prevent premature gelation of collagen I.

2.2. Printing

The printing setup has been described in previous works [13,14]. In summary, to allow firm attachment of the crosslinked hydrogel, the glass coverslips (20×20 mm, 150 μm thick; VWR) were methacrylated. Coverslips were exposed for 15 min at 1 cm to a deep-UV lamp (Novascan PSDP-UV PSD Pro Series Digital UV; Ozone System), incubated for 10 min in a solution of 1% v/v silane methacrylate (3-(Trimethoxysilyl) propyl methacrylate; Sigma-Aldrich) and placed in a dry oven at 120 °C for 1 hour. A 250 μm thick silicone frame (SIN 400 T; Sterne) was fitted around the edges of the coverslip, and a rectangular PDMS pad was placed on top, creating a chamber with a defined height.

Using a positive displacement pipette, the bioink (40 μl) was injected into the chamber (Fig. 1C). Subsequently, the coverslip was placed on top of a standard glass slide fitted under an inverted microscope (IX83; Olympus) equipped with a DMD-based UV patterned illumination device (PRIMO, Alvéole). A pre-defined pattern, provided as a digital grayscale image designed in InkScape (Inkscape Project), was loaded onto the software of the PRIMO device and projected through a 10x objective with UV light at a wavelength of 375 nm, as explained in more detail by Strale *et al.* [16]. The UV dose was calibrated by intensity and curing time to a maximum of 50 mJ/mm^2, and fractions of this dose were applied through specification of the gray value on the design, namely the maximum dose ("High UV", white) or 10% of it ("low UV", dark gray). After printing, each coverslip was transferred to a 6-well plate filled with PBS, where the PDMS pad and silicone frame were manually removed, and any unreacted components of the bioink were washed out with PBS two times for at least 5 min each, at room temperature (RT, approximately 18 to 22 °C). The hydrogel structures remained firmly attached to the methacrylated glass coverslip. For ATR-FTIR experiments, after 72 h of incubation in PBS, hydrogels were fixed for 30 min in 4% formaldehyde solution (Merck), rinsed three times for 5 min each in PBS and 2 times for 5 min each in H_2O, and dried for 24 h.

2.3. Cell culture

All cell types were incubated at 37 °C with 5% CO_2. Primary Limbal-derived Corneal Epithelial Cells (hLCECs) were isolated from human postmortem patients. All procedures conformed to the tenets of the Declaration of Helsinki for biomedical research involving human

Table 1
List of raw materials used for hydrogel formulation.

Material	Abbreviation	Manufacturer& reference	Source	concentration (w/v)		Degree of methacrylation*	Molecular weight* (kDa)
				Stock	final		
Collagen I methacrylate	ColMA	Advanced Biomatrix #5198	Bovine	3%	1%	>20%	~404
Hyaluronic Acid methacrylate	HAMA	Advanced Biomatrix #5212	Bacterial	4%	0.4%	45–65%	100–150
Silk Fibroin methacrylate	SFMA	Matexcel BINK-017	Bombyx mori	10%	2.5%	70–90%	≥100
Lithium phenyl (2,4,6-trimethylbenzoyl) phosphinate	LAP	Advanced Biomatrix #5269	N/A	5%	1%	N/A	N/A

* Data provided by manufacturers.

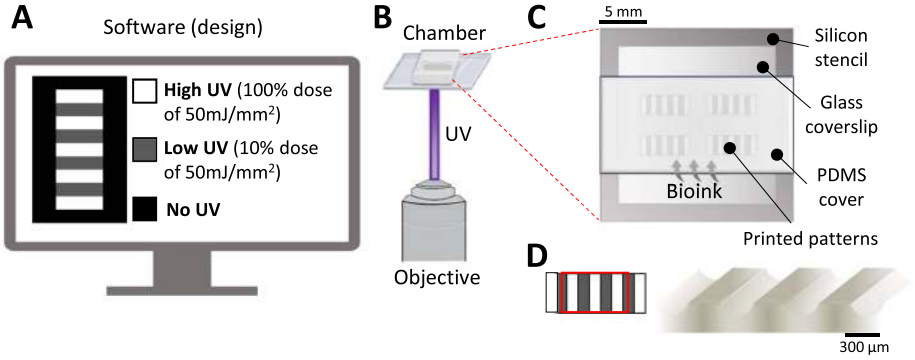

Fig. 1. Experimental process to print gel scaffolds. A) A grayscale design is loaded into the software of the DLP system and is translated into a projection of UV light, transmitted via a Digital Micromirror Device (DMD) through a 10x microscope objective onto a chamber containing the pre-loaded photocurable bioink (B), which within seconds solidifies according to the projected shape. C) The chamber containing the bioink is formed by an underlying glass coverslip and an overlying PDMS pad supported by a silicone frame. D) The produced scaffold used for culture is illustrated, which takes shape after grayscale UV projection induces anisotropic crosslinking densities within the gel and therefore differential swelling dynamics that give rise to this undulating geometry. The red square shows the area of the design corresponding to the illustrated printed scaffold.

subjects. The Agence de la Biomédecine (France) authorized limbus procurement for research (PFS21–013). Limbal cell isolation and amplification were described in a previous work [17]. To summarize, the limbus was harvested from corneoscleral rims and then placed in a balanced salt solution (Alcon) before proceeding with cell isolation. Meanwhile, growth-arrested 3T3-J2 fibroblasts (Kerafast) following Mitomycin C treatment (Merck Millipore) were suspended in DMEM (Gibco) with 10% fetal bovine serum (FBS, Biowest) and seeded at a density of 4.6×10^4 cells/cm^2. The next day, the hLCECs were dissociated (TrypLE Express; Gibco), resuspended in a growth medium (3:1 mixture of DMEM:F12 with 10% fetal bovine serum, (0.4 µg/mL) hydrocortisone, (5 µg/mL) insulin, (1.4 ng/mL) triiodothyronine, (24 µg/mL) adenine, (8.4 ng/mL) cholera toxin, (10 ng/mL) epidermal growth factor and 1% antibiotic-antimycotic (ABAM; Gibco)), and seeded on growth-arrested 3T3-J2 fibroblasts. The medium was changed on the third day and every other day thereafter. After 7 days, the 3T3-J2 feeder cells were detached using Versene (Gibco) and after washes with PBS, hLCECs were dissociated (TrypLE Express) and cryopreserved in DMEM, 20% FBS and 10% DMSO (Sigma-Aldrich). 3T3-J2 feeder cells were only used for initial amplification purposes and not in any other experiment of this study. Two independent male donors, aged 50 and 62 years, were used in this study. As sex-related differences may influence ocular surface biology, the exclusive use of male donors should be acknowledged as a limitation of this study [18].

After printing and washing, hLCECs (passages 2–3) were seeded at a density of 2×10^4 cells/cm^2 on the scaffolds, in KSFM medium (Gibco), supplemented with 1% ABAM. Upon confluency at day 5, the medium was switched to DMEM/F12 (1:1; Gibco) supplemented with 10% FBS, (1.2 mM) Calcium Chloride (CaCl2; Merck), Epidermal Growth Factor (EGF, (10 ng/ml)) and 1% ABAM to induce differentiation and stratification of the epithelial layer. The samples were cultured for up to 3 weeks and the medium was changed every 2–3 days.

All phase contrast images were taken using a CKX53 microscope (Olympus), equipped with a camera (Digital Sight DS-Fi1c, Nikon).

2.4. Fluorescence staining

Samples were fixed in 4% formaldehyde solution for 30 min, permeabilized for 5 min with 0.1% Triton-X (Sigma-Aldrich) in PBS and then placed in blocking solution for 1 hour (5% FBS, 0.05% Triton X-100, 0.05% Tween-20 (Fisher Scientific)) under mild agitation. Primary antibodies (see Table 2) were incubated overnight at 4 °C in blocking solution. After 3 × 5 min washes in PBS with mild agitation, samples were incubated with secondary antibodies for 1 h at RT in blocking solution (see Table 2), counterstained with DAPI (Invitrogen) and, when indicated, stained with Phalloidin-647 (Invitrogen). After 3 × 5 min washes in PBS under mild agitation, samples were mounted onto a microscope glass slide with Permafluor mounting medium (Epredia). The samples were imaged using a confocal microscope (LSM800, Zeiss).

The live/dead assay was performed after 6 h and 24 h of culture on gel scaffolds, using a solution of Calcein AM and Propidium Iodide (see Table 2) in PBS, to label live and dead cells respectively. After 30 min of incubation, imaging was performed by confocal microscopy. For each sample, two Z-stack images covering a significant portion of the scaffold were taken for quantification using the FIJI (ImageJ) software. The percentage of live cells was calculated by dividing the number of live cells by the total number of cells (live + dead).

Table 2
List of reagents for fluorescence staining.

Primary antibody	Species	Manufacturer	Reference	Dilution
Keratin 3/CK3 [AE5](KRT3)	Mouse monoclonal	Abcam	ab77869	1:200
ZO1 (TJP1)	Rabbit polyclonal	Invitrogen	61–7300	1:200
P63 [4A4] (TP63)	Mouse Monoclonal	Abcam	ab735	1:200
Laminin 5 (LAMA3)	Rabbit Polyclonal	Abcam	ab14509	1:200
YAP [63.7] (YAP1)	Mouse Monoclonal	Santa Cruz Biotechnology	sc-101,199	1:200
PAX6	Rabbit Polyclonal	BioLegend	PRB-278P	1:1000

Secondary antibody	Species	Manufacturer	Reference	Dilution
Anti-Mouse IgG (H+L) 488	Goat Polyclonal	Invitrogen	A11001	1:500
Anti-Rabbit IgG (H+L) 555	Goat Polyclonal	Invitrogen	A21428	1:500

Fluorescent dye	Species	Manufacturer	Reference	Dilution
DAPI	N/A	Invitrogen	D3571	1:500
Alexa Fluor™ 647 Phalloidin	N/A	Invitrogen	A22287	1:500
Calcein AM	N/A	Invitrogen	C1430	2μM
Propidium Iodide	N/A	Invitrogen	P3566	500nM

2.5. Image analysis and quantification

Image processing was done using FIJI (ImageJ) software. Determination of P63-positive and PAX6-positive cell ratios was based on measurement of the fluorescent signal intensity of these nuclear markers. All samples were processed in paired fashion (printing, cell culture, immunostaining and image acquisition). For each sample, two representative images from two printed patterns on the same coverslip (each containing both high and low UV-exposed areas) were taken and measured. The analysis was based on 4 μm thick optical Z stack images, merged into a single image by applying an "average projection". These optical sections were taken from 3 different areas of a scaffold: 1) apical cells on an area which received a low UV dose, 2) basal cells of the same area, and 3) the monolayer cells on an area which received a high UV dose. Nuclei were segmented based on pixel intensities of the DAPI signal, and then the region of interest (ROI) of each nucleus was applied to the channel of the marker of interest (P63 or PAX6 staining) to obtain the mean nuclear intensity value of each cell. The threshold of "positivity" was fixed for each independent sample at the 66th percentile of a list of an equal number of randomly selected values from the three different areas (1- apical low UV dose, 2- basal low UV dose, 3- high UV dose).

For the quantification of YAP nuclear/cytoplasmic ratio, for each sample, two representative images from two scaffolds on the same coverslip (each containing both high and low UV-exposed areas) were acquired. Analysis was based on 2.5 μm thick optical Z stack images, merged into a single image by applying an "average projection". Then, based on the DAPI staining, the nuclei were segmented. The ROI of each nucleus was dilated radially by 2 pixels (corresponding to 1.2 μm) and the original nuclear area was subtracted, resulting in a new donut-shaped ROI corresponding to a similar surface area as the nuclear area, but representing the cytoplasmic (perinuclear) region of the cell. The cytoplasmic and nuclear ROIs were applied on the YAP channel to extract the signal intensity of the nucleus and cytoplasm of each cell. The nuclear/cytoplasmic ratio was calculated by dividing the two values (nuclear and cytoplasmic) for each cell (data point), and all data points were then averaged into a single representative mean value for the condition of interest.

Background noise was quantified by selecting 5 random areas devoid of cells per image, and the mean background values were subtracted to values of interest. High UV-exposed and low UV-exposed regions of the scaffold had different levels of autofluorescence, so, for YAP staining quantification, distinct background intensities were quantified per image.

For the quantification of epithelial thickness (Fig. 4D), each image/sample was sagittally sectioned (orthogonal projection) into three different 70 μm thick optical stacks. Within each section, measurements were taken at three equally spaced positions and plotted as signal intensity (DAPI) against distance (in pixels). The epithelial thickness was determined by the width of the DAPI signal peak, which was clearly distinguishable from the background signal. This pixel distance was then converted to micrometers using calibrated image metadata.

2.6. Scanning electron microscopy

hLCECs seeded on printed scaffolds were fixed after 24 h in a solution of 2% paraformaldehyde (Thermo Fisher Scientific), 2.5% glutaraldehyde (Alfa Aeasar) in sodium cacodylate at pH 7.3 (Acros Organics). After washing in cacodylate buffer, samples were dehydrated through a graded concentration of ethanol from 30% to 100% and critical point dried (Leica). Samples were mounted on 12 mm SEM stubs, sputtered with 4 nm of platinum (Leica) and imaged using a field emission gun scanning electron microscope (GeminiSEM300, Carl Zeiss) with an acceleration voltage of 2 keV under high vacuum. Secondary electrons were collected. Scan speed and line averaging were adjusted during observation. Images were not processed further.

2.7. Mechanical testing and swelling assay

The Young's (elastic) modulus of photopolymerized hydrogels was determined using the Microtester G2 (CellScale). Individual square 2 × 2 mm gel pads were printed at 100% or 10% of 50 mJ/mm^2, for high and low UV respectively, with an initial thickness after printing of 250 μm. It is important to note that the square pads printed at low and high UV doses were tested separately, as our setup did not allow accurate measurement of the two conditions in a patterned context. Measurements were performed at RT or 37 °C, after overnight incubation in the respective temperature, to reach equilibrium. Force and displacement data upon compression (1 μm.s^{-1} rate) were collected and converted into a stress-strain curve. The Young's modulus (E) was calculated from the linear region of the stress-strain curve (ranging from 5–15% strain), from the average value of five compressive cycles, where $E = \sigma/\varepsilon$ (σ = stress = force/area; ε = strain = % of displacement from original gel height). Following the manufacturer's recommendation, we tailored each gel condition to a different cantilever, while accounting for the diameter of the cantilever in the equations relating to applied force, therefore normalizing to a certain degree the obtained values.

2.8. ATR-FTIR

Attenuated Total Reflection Fourier-Transform InfraRed (ATR-FTIR) spectra were recorded at the SMIS beamline of synchrotron SOLEIL (Saint Aubin, France) using a ThermoFisher Scientific Nicolet 5700 FTIR spectrometer equipped with a Smart MIRacle ATR accessory, a KBr beamsplitter and a DTGS detector. The ATR accessory was equipped with a 2 mm single bounce diamond Internal Reflection Element (IRE). Spectra were collected at 4 cm^{-1} resolution between 600 and 4000 cm^{-1}, averaging 128 scans. Spectra were preprocessed in Omnic 7.2 with the Atmospheric suppression routine and Automatic smoothing. Spectra were analyzed with Quasar 10.

2.9. Statistical analysis

All data was analyzed on GraphPad Prism 10. Each experiment represents at least three independent samples (as indicated in each Figure), and all values are expressed as the mean ± standard deviation.

Statistical significance was assessed with a Student's *t*-test (paired, parametric), with $p < 0.05$ considered to be statistically significant.

For the data on YAP nuclear/cytoplasmic localization, extreme outliers were removed with the ROUT method (Q = 0.1%) and a Kolmogorov-Smirnov test was performed (unpaired, non-parametric), with $p < 0.05$ considered to be statistically significant.

3. Results

This study aimed to develop a robust limbal corneal model that supports long-term growth and differentiation of limbal epithelial cells while addressing the scalability versus complexity challenge in tissue engineering. To this end, we developed an innovative single-step bioprinting methodology based on the hypothesis that photocurable bioinks can undergo predictable shape changes without multiple processing steps. We employed Digital Light Processing (DLP), a maskless photolithography technology with the ability to fine-tune projected UV with spatiotemporal sensitivity [16]. It allowed us to create scaffolds with spatially heterogeneous crosslinking densities.

3.1. Attachment and growth of human primary limbal-derived corneal epithelial cells on printed scaffolds were favored by the addition of silk fibroin methacrylate in the bioink composition

The grayscale design shown in Fig. 1 represents the digital mask used in this study. This UV projection pattern is a 2700×1000 μm rectangle composed of 9 alternating stripes, where 5 white stripes translate to "high" UV dose, and 4 light grey stripes to a "low" UV dose (100% and 10% of 50 mJ/mm^2, respectively). The design dimensions were selected to reflect key limbal anatomical principles. The stripe length (1 mm) approximates the radial width of the human limbus, while the stripe width (300 μm) was based on previous palisade-of-Vogt–mimicking studies [8–10].

The primary objective of this study was to determine the optimal bioink formulation for DLP bioprinting that allowed hLCEC adhesion and growth. Several combinations of methacrylated polymers were exposed to the above UV grayscale pattern. Initially, ColMA alone, HAMA alone and the combination of ColMA and HAMA (hereafter referred to as "CH") enabled good printability (Fig. 2A, Day 0) over a

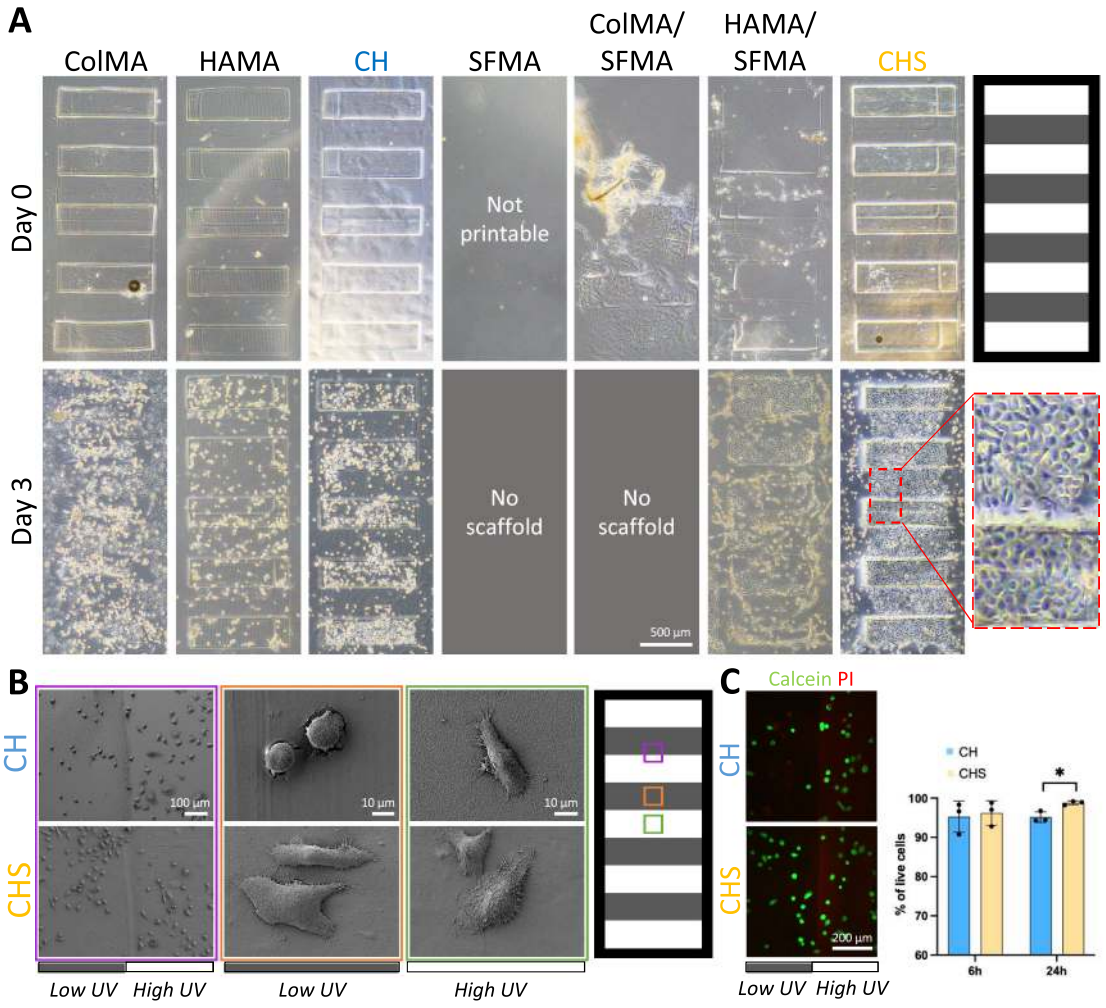

Fig. 2. Silk Fibroin Methacrylate influences primary human Limbal-derived Corneal Epithelial cell (hLCEC) attachment and growth. A) Representative phase contrast microscopy images showing printing efficiency of scaffolds photopolymerized from bioinks of various formulations (top panel) and hLCEC adhesion and growth 3 days post-seeding (bottom panel) on the same scaffolds. The scaffolds were printed according to the design shown on the left panel (white stripes represent 100% of max UV dose and dark gray 10% of max UV dose). CH consists of ColMA (1%w/v) and HAMA (0.4%w/v), while CHS consists of ColMA (1%w/v), HAMA (0.4%w/v) and SFMA (2.5%w/v). Red dashed square highlights the area in higher magnification, represented at the bottom right. B) Scanning electron microscopy representative images showing the spreading of hLCECs seeded at low density, on scaffolds with (CHS) or without SFMA (CH) 24 h post-seeding, on areas of the gel exposed to a high UV dose (white bars) and at low UV dose (dark gray bars). Colored squares represent the area of the image on the scaffold. C) Representative fluorescent microscopy images of a live/dead assay of hLCECs 24 h post-seeding on scaffolds with (CHS) or without SFMA (CH) (live cells: calcein, green and dead cells: propidium iodide, red) and quantification at 6 h and 24 h. n = 3. ColMA: Collagen Methacrylate, HAMA: Hyaluronic Acid Methacrylate; SFMA: Silk Fibroin Methacrylate; CH: ColMA + HAMA; CHS: ColMA + HAMA + SFMA. * $p < 0.05$.

wide range of concentrations and ratios (data not shown). However, hLCEC seeding on these scaffolds resulted in very low cell attachment and growth after 3 days of cell culture, on all tested formulations. In phase contrast microscopy images, cells remained small, round and highly refractive, characteristic of cells with impaired attachment and spreading (Fig. 2A, Day 3). On the ColMA scaffold, some cells appeared to be attached and spread on the high UV exposed areas, but these areas were deformed compared to their post-printing state. On the HAMA

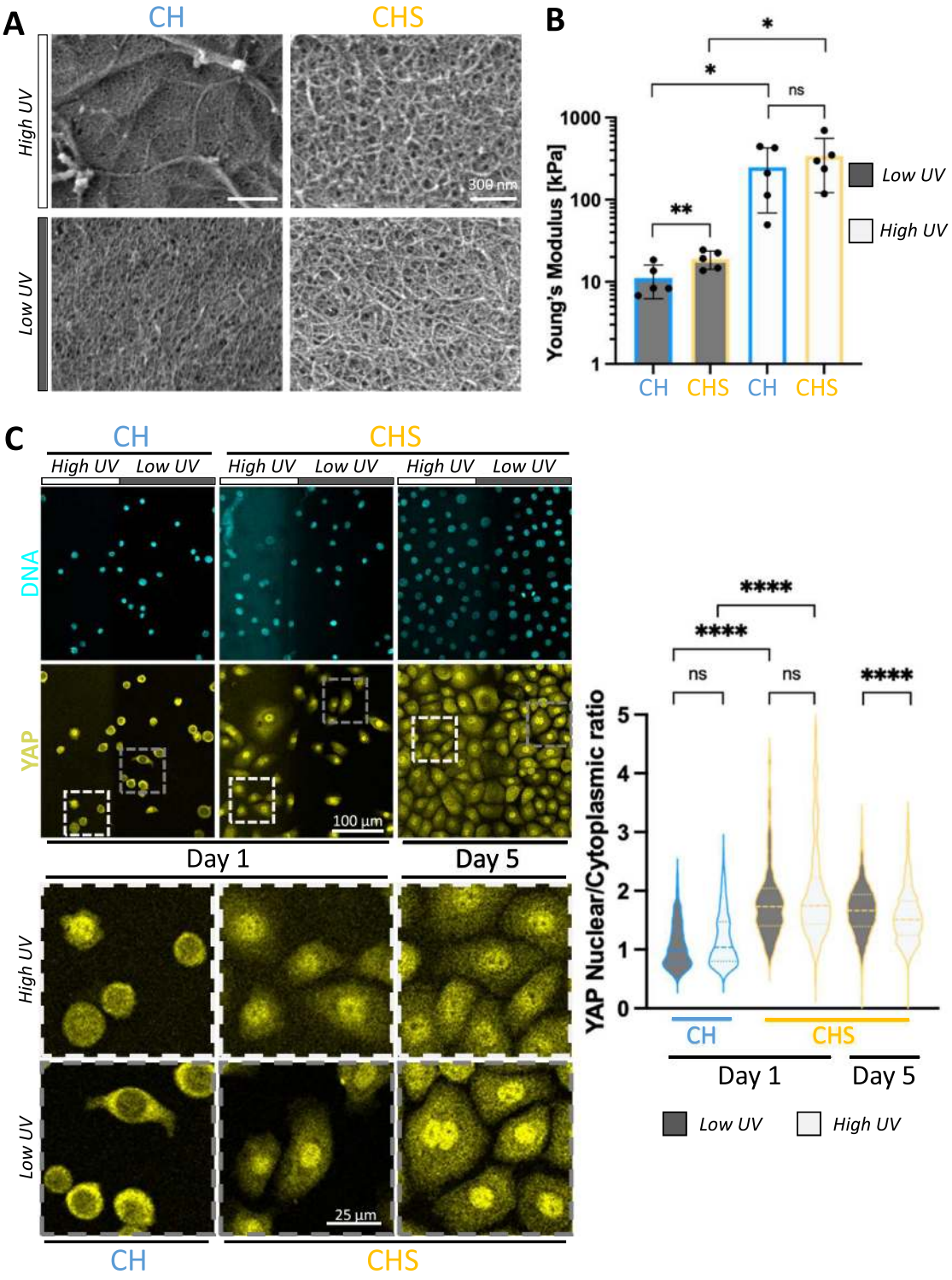

Fig. 3. Silk Fibroin Methacrylate induces structural hydrogel modification and photocrosslinking confers mechanical changes, both of which correlate with YAP translocation. A) Representative scanning electron microscopy images showing the surface microtopography of scaffolds with (CHS) or without (CH) SFMA. B) The Young's modulus of scaffolds with (CHS) or without (CH) SFMA, and as a function of UV dose, 24 h post-printing in PBS at 37 °C. n = 5. C) Representative confocal images of YAP immunostaining on hLCECs, seeded on scaffolds with (CHS) or without (CH) SFMA, at high and low UV dose conditions, after 1 and 5 days (for CHS) in culture. Each image includes adjacent regions of high and low UV exposure. White (high UV) and grey (low UV) dash squares highlight areas in higher magnification, represented in the lower panel. Nuclear DNA was stained with DAPI. Violin plots show the quantification of YAP nuclear/cytoplasmic ratio. n = 4 independent experiments, 1421 cells quantified in total for day 1, and 3850 for day 5. ns: non-significant; * $p < 0.05$; ** $p < 0.01$; **** $p < 0.0001$.

scaffold, all cells remained round and refractive. On the low-UV exposed area of the CH scaffold, cells remained round and refractive, as observed in phase contrast microscopy images. SEM images provided additional details: cells on CH scaffolds in low UV exposed areas were visibly attached but maintained a round shape (Fig. 2B). In contrast, cells on high UV-exposed areas exhibited a spread morphology, characterized by a larger surface area, flatter appearance, and the presence of filopodia (Fig. 2B).

Since collagen and hyaluronic acid, either alone or combined, failed to support efficient cell adhesion, we next examined methacrylated silk fibroin (SFMA) as a potential additive to our bioink [19,20]. Initially, to achieve optimal printability of SFMA alone by DLP, concentrations above 10% had to be used but cells were unable to adhere to this substrate (Supplemental Figure 1A). At lower concentrations, SFMA did not produce any recognizable patterns (Fig. 2A, Day 0). In combination with ColMA and HAMA however, after screening a range of ratios and concentrations, we found that the triple formulation of ColMA, HAMA and SFMA (now referred to as "CHS") enabled consistent printability with scaffolds closely matching the digital mask at various concentrations (10% to 1% w/v of SFMA with ColMA at 1% w/v and HAMA at 0.4% w/v). Notably, while ColMA alone, HAMA alone and the CHS combination enabled consistent printability with scaffolds closely matching the digital mask, the combination of SFMA with either ColMA or HAMA was not suitable for DLP bioprinting as they did not produce robust patterns (Fig. 2A, Day 0).

Interestingly, the (1% ColMA/0.4% HAMA/2.5% SFMA) "CHS" formulation promoted hLCEC attachment and spreading (Fig. 2A, Day 0 and Day 3; supplemental Figure 1A and 1B). In the following, CHS now refers to the above composition, and CH refers to the 1% ColMA/0.4% HAMA formulation. After 3 days of culture, phase contrast microscopy images revealed confluent and non-refractive hLCECs on both high and low UV-exposed areas, indicating effective attachment and growth compared to cells on the CH scaffold. On SEM images, cells exhibited a spread morphology with formation of lamellipodia and filopodia, in both low and high exposed areas. Additionally, hLCEC viability was high on both CH and CHS scaffolds at 6 h and 24 h post-seeding, suggesting that the deficit in adhesion and growth on CH scaffolds was not due to any initial toxicity linked to printing settings or gel composition (Fig. 2C). In summary, these results demonstrated that the triple CHS formulation, printed using the striped digital mask by DLP at both high and low UV doses, was a suitable substrate for hLCEC adhesion and growth.

Interestingly, on CH and CHS scaffolds, we also seeded other cell lines (corneal, hepatic and bronchial immortalized cell lines) to compare their behaviors with hLCEC (Supplemental Figure 2). Both hTCEpi and HLCE corneal epithelial cell lines exhibited the same behavior as primary hLCECs. BEAS-2B bronchial cells, however, attached, spread and grew better on CH scaffolds compared to CHS scaffolds, while HepaRG hepatic cells displayed similar behavior on both CHS and CH scaffolds. These results suggest that the improved corneal cell adhesion and growth observed on the CHS formulation is cell type specific.

3.2. Influence of silk fibroin methacrylate on hydrogel scaffold properties

To explore the impact of SFMA on hydrogel properties that could enhance corneal epithelial cell growth, we first performed SEM imaging to observe the structure of scaffolds with and without SFMA (Fig. 3A). The images revealed qualitative differences between the two scaffolds, particularly in surface topography. The fibrils on CHS scaffolds were more pronounced and spaced out, with a higher contrast indicating a broader range of feature sizes.

Next, we assessed the influence of SFMA on scaffold stiffness (Fig. 3B). At 37 °C, CHS scaffolds exhibited a higher Young's (elastic) modulus compared to CH scaffolds at low UV dose (x1.7; CHS = 19 kPa, CH = 11 kPa), while the difference was not statistically significant at high UV doses (CHS = 340 kPa, CH = 249 kPa) (Fig. 3B). High UV dose had a dramatic effect on stiffness, regardless of the combination used.

Interestingly, in contrast to measurements done at 37 °C, CHS scaffolds at RT and lower UV dose were significantly softer than their CH counterparts and CHS at 37 °C (at RT, low UV dose, CHS = 6 kPa and CH = 21 kPa, while at high UV dose, CHS = 273 kPa and CH = 331 kPa), whereas CH scaffold stiffness remained similar at both RT and 37 °C (Supplemental Figure 3A).

Notably, from a corneal bioengineering perspective, the CHS combination remained transparent in high and low UV exposed areas, even after 3 weeks of culture (supplemental Figure 4A and B) and was robust enough to withstand manipulation with forceps (supplemental Video 1).

3.3. Gel composition and crosslinking modulate mechanotransduction signaling

To investigate the influence of substrate properties on cellular response, we analyzed the nuclear/cytoplasmic localization of YAP, a protein known to sense and transduce mechanical signals [21], and for its involvement in LESC homeostasis [15,22]. We observed that hLCECs seeded and grown for 24 h on CHS scaffolds exhibited a significantly higher nuclear/cytoplasmic ratio of YAP compared to CH scaffolds, regardless of whether the cells were on high or low UV dose areas on the scaffold (representing stiff and soft substrates respectively) (Fig. 3C, Day 1). On the other hand, we did not observe a statistically significant difference in the YAP nuclear/cytoplasmic ratio between cells on stiff and soft areas of the same scaffold formulation 24 h post cell seeding (CH or CHS respectively) (Fig. 3C).

It is worth highlighting that after 5 days of culture in growth medium, on CHS scaffolds, cells formed a confluent monolayer regardless of the UV exposure of the substrate. Cells grown on low-UV dose areas, corresponding to the softer substrate, retained a significantly higher YAP nuclear/cytoplasmic ratio than cells on high-UV dose areas corresponding to the stiffer area of the scaffold (Fig. 3C, Day 5).

3.4. Alternating UV exposures generate undulating architecture in silk fibroin containing scaffolds via a shape morphing process

Our initial hypothesis was that spatially controlled UV crosslinking of the bioink would induce a predictable and programmable shape transformation of the scaffold. Immediately after printing, low-exposed regions of CHS scaffolds exhibited enhanced swelling compared to high-exposed regions (Fig. 4A, h1). However, upon placing the scaffolds at 37 °C, this phenomenon reversed (Fig. 4A, d1, d14), as the volume of low exposed regions decreased and formed "grooves" between the (now thicker) high UV exposed regions. On scaffolds bearing cells, we observed that the depth of the grooves, measured between the top of the ridge and the bottom of the groove, increased progressively from day 1 to day 21, reaching a maximum of approximately 26 μm at day 14 (supplemental Figure 5A). Conversely, the width of the grooves and the ridges remained stable over 21 days (supplemental Figure 5B). This resulting undulating architecture was not observed at RT (supplemental Figure 3B). Additionally, the undulating topography could not be reproduced with CH bioink (supplemental Figure 3B).

To investigate the molecular basis of this temperature-dependent shape transformation, ATR-FTIR spectroscopy was performed on fixed and air-dried CHS and CH scaffolds subjected to the four experimental conditions (Low vs High UV, RT vs 37 °C for 72 h). It revealed an increase in β-sheet content, evidenced by a typical growing absorption band at 1620 cm^{-1}, in CHS scaffolds incubated at 37 °C (Supplemental Figure 6A). This β-sheet formation was absent in CH scaffolds under all conditions tested (Supplemental Figure 6B), demonstrating that it is strictly dependent on the silk fibroin component (Supplemental Figure 6A–D). Quantification of the β-sheet/α-helix ratio by peak area integration confirmed that 37 °C incubation significantly increased β-sheet content compared to RT in both low UV (x3.4 fold increase, $p < 0.01$) and high UV (x1.7 fold increase, $p < 0.0001$) conditions (Fig. 4B

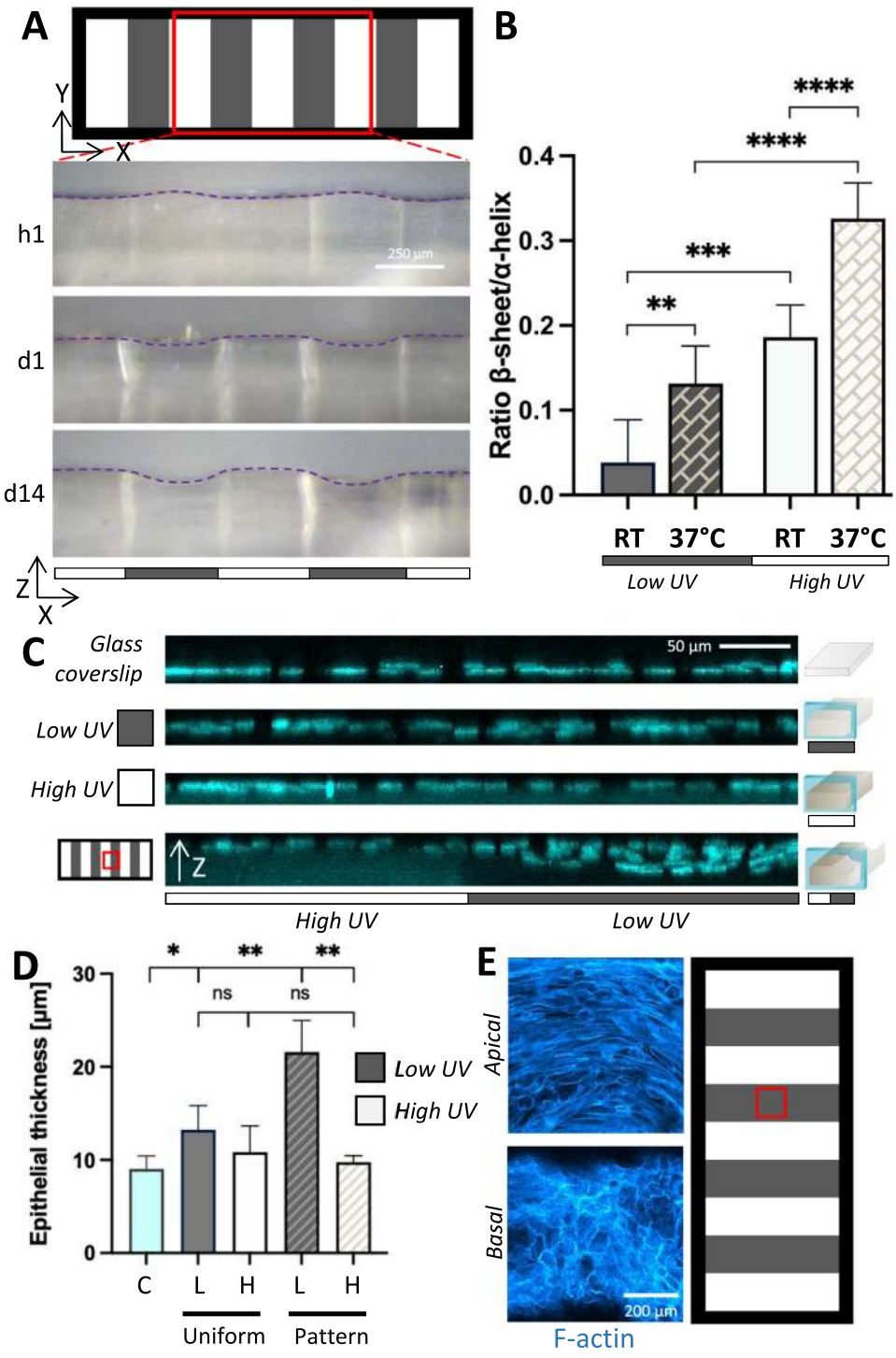

Fig. 4. Grayscale UV projection triggers shape morphing of scaffolds into undulating topography. A) Sagittal views of the scaffolds showing alternation of high (represented in white) and low (represented in grey) UV dose was applied to the bioink, where low-exposure areas exhibited more advanced shrinking over time at day 1 (d1) and day 14 (d14), despite initial swelling 1 hour post-printing (h1). This phenomenon created a wavy surface. The red square represents the area of the image on the scaffold. B) β-sheet/α-helix ratio in CHS scaffolds exposed to a uniform low or high UV dose and incubated for 72 h at Room Temperature (RT) or 37 °C. Spectra were normalized on the intensity of the amide I band at 1656 cm^{-1}. n = 3 C) Representative confocal images displayed in orthogonal projection (70 µm in Y axis) of hLCECs grown for 14 days on glass, on scaffolds exposed to a uniform low or high UV dose, and scaffolds with alternation of areas exposed to low and high UV level. Nuclear DNA stained with DAPI. D) Epithelial layer thickness quantification based on DAPI staining. "Uniform" refers to scaffolds printed with a single uniform UV dose, "pattern" refers to scaffolds printed with alternation of high and low UV doses, C: glass coverslip, L: Low UV dose, H: High UV dose. n = 4 per condition from 2 independent cell donors. E) Representative confocal images of basal and apical hLCECs stained with phalloidin (F-actin cytoskeleton) on areas exposed to low UV, after 14 days of culture on scaffolds with alternation of areas exposed to low and high UV dose. The red square represents the area of the image on the scaffold. ns: non-significant; * $p < 0.05$; ** $p < 0.01$; *** $p < 0.001$; **** $p < 0.0001$.

and supplemental figure 6E). High UV exposure further amplified this increase compared to low UV at 37 °C.

Collectively, these results establish that spatially controlled UV crosslinking combined with the temperature-responsive properties of silk fibroin-containing bioink produces predictable and programmable 3D shape transformation, associated with increased β-sheet formation upon incubation at 37 °C. The digital mask used allows the generation of scaffolds with a wavy surface. As we have established that CHS scaffolds provide the most appropriate substrate for our purpose, the rest of this study deals exclusively with this formulation.

3.5. 3D-engineered scaffold topography enables local corneal-limbal epithelial cell stratification and tissue organization

Upon induction of an undulating topography, we looked more closely at the interaction of corneal epithelial cells with these different scaffold topographies, particularly in terms of stratification. Remarkably, cells stratified more extensively on areas exposed to low UV doses that formed grooves within patterned (undulating) scaffolds, while the stratification remained more limited on areas exposed to a high UV dose within patterned scaffolds ($p < 0.01$) (Fig. 4C lower panel and Fig. 4D). The extent of stratification depended on the depth of the local undulation; at the apex of low exposed areas, cells would meet those of the adjacent ridge, forming a relatively smooth planar continuum of cells, while at the bottom the thickness of the epithelium varied according to the undulations of the underlying substrate. Upon decoupling topography from stiffness by producing isolated flat soft gels, we observed that the cells did not significantly stratify, despite a slight increase in epithelium thickness on low-UV dose gels compared to the glass coverslip control ($p < 0.05$) (Fig. 4C and 4D). Nevertheless, where stratification was present in topographical grooves of low UV dose-exposed areas, F-actin staining revealed that upon stratification, epithelial cells exhibited a distinct morphology along the Z-axis. Basal cells displayed a compact, rounded structure, while apical cells showed a more spread, elongated morphology (Fig. 4E).

3.6. Local stratification on 3D-engineered scaffold topography was accompanied by apico-basal cell organization and expression of immaturity and differentiation markers in a physiologically-relevant manner

Following our results showing stratification and morphological changes based on topography, we mapped relevant markers that normally exhibit location-specific expression (Fig. 5A). In the corneal tissue, P63 is expressed in basal limbal epithelial immature cells [23,24] and PAX6 is one of the earliest corneal epithelial differentiation markers, expressed in suprabasal and superficial cells [9,25]. After 14 days of culture, we observed that P63-positive cells were mostly found in the

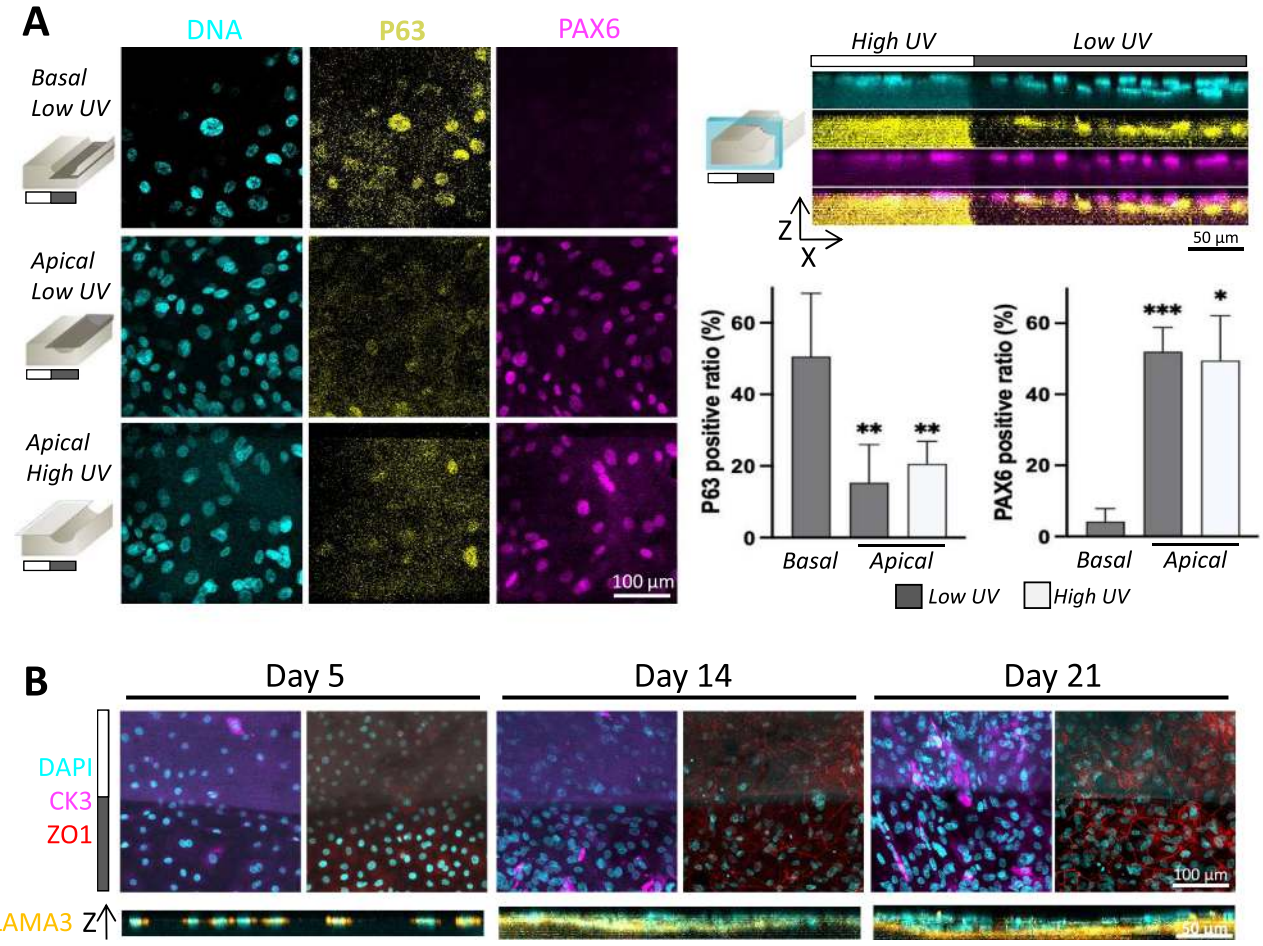

Fig. 5. Stratification of cells on topographical hydrogel scaffolds is followed by functional organization. A) Representative confocal images of hLCECs immunostained for P63 and PAX6, at the apical and basal layers, after 14 days of culture on scaffolds with alternation of low and high UV dose areas (left panel). Representative images in orthogonal view (top right panel). Quantification of P63 and PAX6 positive cells at basal and apical layer on low and high UV dose areas (bottom right panel). n = 6 for P63 and n = 4 for PAX6. *$p < 0.05$, **$p < 0.01$, ***$p < 0.001$. B) Representative confocal images of areas covering both high and low UV dose areas, showing a gradual increase in expression of differentiation markers (ZO-1, CK3) up to day 21. An orthogonal projection of a local crypt-like undulation of a low UV dose area also shows parallel increase of Laminin 5 (LAMA3) expression, a basement membrane component.

basal layer of the stratified epithelium of low-UV exposed areas, with more than half of the cells (~51%) exhibiting positive P63 staining. At the apical layer of low UV exposed areas and in high-UV exposed areas, a significantly lower proportion of P63 positive cells was observed (~15% and ~21% respectively; $p < 0.01$) (Fig. 5A). Conversely, PAX6-positive cells were predominantly found at the apical layer of low-UV exposed areas (~52%) and at high-UV exposed areas (~49%), while basal cells of low-UV exposed areas showed very low expression (~4%; $p < 0.001$) (Fig. 5A). No overlap between the two markers was detected within individual cells, and orthogonal views revealed a distinct layering of P63 and PAX6 positive cells (Fig. 5A).

The model was maintained in culture over a period of 21 days and demonstrated systematic differentiation patterns with a basal-apical gradient, with immature cells in the basal layer, and differentiation toward apical cells. The CK3 differentiation marker, naturally found in the central cornea and suprabasal limbus [9,26,27], gradually increased (Fig. 5B). In parallel, the tight junction protein ZO-1 [28,29] gradually organized as a mesh, demonstrating the organization of the barrier function of the epithelium. Lastly, in orthogonal projections, we observed the production and progressive organization of Laminin 5, a ubiquitous BM component (Fig. 5B, bottom panel). This marker of BM maturation not only increased over time but also displayed a progressively sharper linear pattern.

4. Discussion

Creating a minimal yet suitable environment for the differentiation, growth, and ideally the self-renewal of human limbal-derived corneal epithelial cells remains challenging in corneal tissue engineering. Many groups have successfully published elegant and functional 3D models to grow limbal epithelial cells using various technologies such as molding [9], microstereolithography [8], or two-photon polymerization [10]. However, most of these systems remain technologically demanding, time-consuming, requiring multi-step fabrication, or low-throughput workflows that limit scalability. Furthermore, while several models have achieved short-term epithelial stratification or transient progenitor maintenance, very few enabled the long-term coexistence of progenitor and differentiated cells together with progressive BM maturation in a minimal epithelial-only context. Our bioprinting approach coupled with shape morphing hydrogel [30,31] should facilitate the scalability of bioprinting 3D scaffold substrates with complex topographies for advanced *in vitro* modeling. The platform uses a DLP bioprinter [16] to project UV light based on a digital mask (alternating stripes at 100% and 10% of 50 mJ/mm^2) into a volume of bioink composed of methacrylated collagen, hyaluronic acid and silk fibroin (CHS) on methacrylated glass coverslips. Following UV exposure and washing, the hydrogel undergoes programmed 3D deformation at 37 °C, creating an undulating topography. The depth of the grooves increased progressively over 21 days, whereas the widths of both the grooves and ridges remained stable. We hypothesize that the stiffer ridges, which present a greater UV-exposed area, act as structural "pillars" that resist lateral contraction of the grooves; consequently, the grooves contract vertically, giving rise to the observed undulations. The stability of groove and ridge dimensions in cell-seeded scaffolds, further suggests that scaffold degradation over this period is minimal. The groove depth reached an average maximum of 26 μm, which remains below the ~70 μm reported for human native limbal crypts [9]; nevertheless, optimization and fine-tuning of the system will investigate whether the design can more closely approach native dimensions, further improving the system.

This shape transformation appears to be driven by silk fibroin. In fact, scaffolds composed only of methacrylated collagen and hyaluronic acid exhibited printability similar to CHS scaffolds when exposed to UV according to our digital mask, but remained flat at both RT and 37 °C. The same was observed for CHS scaffolds at RT, suggesting temperature-sensitive behavior specific to silk fibroin. Higher temperature is known to trigger a transition in the secondary molecular structure of silk fibroin, with unraveled random coils turning into compact β-sheets [19,32]. This conformational change is accompanied by water expulsion due to hydrophobicity and reduction of steric freedom and free volume [33]. Using ATR-FTIR, we confirmed that scaffolds exposed to high and low UV doses exhibit an increase in β-sheet content at 37 °C compared to RT (x3.4- and x1.7-fold increase, respectively). Of note, β-sheet content was also higher in highly crosslinked regions at both RT and 37 °C. The photopolymerization of methacrylate groups by LAP is an exothermic reaction that generates local heat transiently during crosslinking [34], which may contribute to the initial nucleation of β-sheet structures in silk fibroin. Beyond this thermal effect, covalent crosslinking polymers are known to directly promote β-sheet formation in silk fibroin by restricting chain mobility and reducing the free volume available to protein segments, thereby lowering the energetic barrier for the random coil-to-β-sheet conformational transition [35]. Scaffold regions exposed to high UV doses displayed the highest β-sheet formation, yet did not undergo any detectable shape transformation. This apparent paradox may be explained by two non-exclusive mechanisms: first, higher stiffness of the fully crosslinked network may resist the contractile forces generated by β-sheet formation, preventing their translation into macroscopic deformation; second, the high UV dose may already drive substantial β-sheet formation during the printing process itself, such that the additional conformational change occurring upon 37 °C incubation is insufficient to generate the volumetric differential required for shape transformation (x1.7 fold increase in β-sheet formation between RT and 37 °C).

In this model we also observed, as expected, that stiffness was primarily influenced by UV dose, with higher doses yielding stiffer hydrogels regardless of bioink composition. However, at low UV dose and RT, CHS scaffolds were significantly softer than CH scaffolds. This apparent softness can be explained by the conformational state of silk fibroin under these conditions. As confirmed by ATR-FTIR, SFMA remains in a predominantly random coil conformation at RT and low UV dose, contributing negligible physical crosslinking to the network. In this amorphous state, the addition of SFMA may also dilute the covalent crosslinking density available to ColMA and HAMA, resulting in a less dense network compared to CH alone. At 37 °C however, CHS scaffolds became stiffer than their CH counterparts, consistent with the β-sheet crystallization observed by ATR-FTIR, as it is well established that physical crosslinks from silk β-sheet domains are an important determinant of silk fibroin hydrogel stiffness [32,36].

The literature on corneal mechanical properties is notoriously heterogeneous, reflecting differences in measurement methodology, loading mode, strain range, hydration state, and tissue anisotropy, making direct numerical comparisons difficult. Nevertheless, order-of-magnitude estimates and regional trends (central vs. peripheral/limbal) can still be informative. Reported values of Young's modulus span a wide range, from 0.1 to 57 MPa [37], though more clinically relevant low-strain, *in vivo* measurements generally fall between 0.2 and 1 MPa, with a mean of 0.25 ± 0.10 MPa reported across 100 healthy human corneas *in vivo* [38]. From our own preliminary experiments, *ex vivo* measurements on human central corneas yielded a value of approximately 0.3 MPa ($n = 2$; data not shown), consistent with this range. Collectively, these central cornea values are of a similar order of magnitude to those measured on our high UV-exposed CHS gels. Data on limbal elasticity specifically is more limited; however, Eberwein *et al.* [39] measured human corneoscleral rims by nanoindentation and reported a Young's modulus of approximately 10 kPa for the limbal region, a value that aligns closely with our low UV-exposed CHS gels.

Beyond its role in shape morphing, silk fibroin also proved essential for cell adhesion. While methacrylated collagen and hyaluronic acid (either alone or in combination) printed well, they failed to support cell attachment and growth. Cells remained small, round, and highly refractive after three days regardless of UV dose. Addition of silk fibroin to the bioink enabled hLCECs attachment and growth [40], with cultures maintained for at least three weeks, matching or exceeding previously

published models. This is particularly interesting given that biosourced silk fibroin from *Bombyx mori* lacks conventional cell-binding motifs such as RGD. Scanning electron microscopy revealed that CHS scaffolds had a rougher substrate with more pronounced and spaced-out fibrils, which could promote cell attachment and growth by providing a larger surface area and offering more binding sites for cell adhesion [41].

Upon adhesion and growth until confluency of hLCECs, the medium was switched to favor differentiation. On any flat gel scaffold, whether cured by uniform high or low UV dose, as well as on glass coverslips, stratification was very limited with no more than two cell layers. However, within undulating scaffolds, cells stratified more extensively on areas exposed to low UV doses (softer areas that formed grooves) reaching up to five layers, while stratification remained very limited on areas exposed to a high UV dose (stiffer areas that formed ridges) within the same scaffolds. Taken together, these observations show that reduced stiffness alone is not sufficient to induce stratification in our system and undulation is necessary, but we cannot rule out that a softer substrate in grooves also participates in epithelial stratification [42–44]. Although a fully stratified epithelium comparable to native limbal tissue was not achieved, the present model using primary epithelial cells successfully recapitulated epithelial differentiation, BM maturation, and the persistence of progenitor cells. Among the strategies being considered to further promote stratification, epithelial–stromal crosstalk will be introduced through the encapsulation of corneal stromal cells within the scaffold, as discussed further below. Additionally, air-lifting will be implemented to better recapitulate the ocular surface microenvironment and further promote differentiation and stratification.

The influence of substrate properties on cellular response was further investigated by analyzing the nuclear/cytoplasmic localization of YAP, a co-activator known, among other functions, to transduce mechanical signals [21]. After 24 h, hLCECs seeded on CHS scaffolds exhibited a significantly higher nuclear/cytoplasmic ratio of YAP compared to CH scaffolds, regardless of whether cells were on high or low UV dose areas. Two interpretations can account for this observation. On one hand, intrinsic gel properties such as porosity and surface topography in the CHS composition may provide additional mechanosensing cues that promote early YAP nuclear translocation. On the other hand, cells at 24 h post-seeding on CH scaffolds may retain a more rounded morphology with limited spreading, a cellular state that is inherently associated with cytoplasmic YAP retention irrespective of substrate stiffness [45]. However, after five days of culture on CHS scaffolds, when the epithelium is confluent and monolayered, cells on low-UV dose areas (softer substrate) retained a significantly higher YAP nuclear/cytoplasmic ratio than cells on high-UV dose areas (stiffer substrate). This shift likely reflects cell-matrix interactions, as a stiffness gradient is well established as a regulator of YAP signaling [15,46–48]. This observation is in accordance with recent studies demonstrating that LESCs on a soft substrate display a nuclear localization of YAP. The effect of substrate rigidity on YAP localization is cell-type dependent; canonically, reports of YAP nuclear localization correlated with cells on stiff substrates [21]. On LESCs, elevated nuclear YAP on softer substrates has been associated with maintenance of an undifferentiated state both *in vitro* and *in vivo* [15]. Corneal limbal epithelial cells with nuclear YAP localization have been shown to display high proliferative capacity and increased P63 expression [15]. This underscores the critical role of substrate biomechanics in regulating YAP localization and consequently LESC stemness.

In our system, stratification was accompanied by functional organization. After 14 days of culture, PAX6 and P63-positive cells were quantified at the apical and basal layers of stratified epithelium in order to assess differentiated corneal epithelial cell fate and progenitor-competent cells respectively. P63-positive cells were mostly found in the basal layer of the stratified epithelium at low-UV exposed areas (soft grooves). On the apical layer of the grooves and on the ridges (high-UV exposed, stiff areas, with monolayered epithelium), a significantly lower proportion of P63-positive cells was observed. Conversely, PAX6-positive cells were predominantly found at the apical layer of the grooves and ridges. The model was maintained in culture over a period of 21 days and demonstrated systematic differentiation patterns with a basal-apical gradient and no overlap between P63 and PAX6 within individual cells. The arrangement of progenitors at basal levels and differentiated cells at apical levels follows native limbal tissue organization [49]. It is worth noting that P63 expression was enhanced but not limited to the low-UV exposed regions, as reported before for the limbal niche [50]. Additionally, the CK3 corneal differentiation marker expression gradually increased over the 3-week period and in parallel the tight junction protein ZO-1 gradually organized as a mesh, demonstrating the organization of the barrier function of the epithelium. Importantly, we also observed the production and progressive organization of laminin-5, a ubiquitous BM component. This marker of BM maturation not only increased over time but also displayed a progressively sharper linear pattern. BM maturation has scarcely been described in epithelial cell culture systems, as the accumulation of BM proteins usually requires complex epithelial-stromal-endothelial interactions [51,52].

The long-term coexistence and spatial organization of progenitors and mature cells in our model, along with *de novo* production of BM-specific components and barrier function creates a biologically relevant advanced limbal *in vitro* system that supports “native-like” tissue development and organization. While our undulating architecture differs from other models, it yields interesting outcomes in terms of epithelial cell behavior and BM maturation. From a technological standpoint, the single-step DLP procedure, coupled with silk-based photocurable bioink, allows reproducibility and precise control of scaffold properties: local topography, shape and stiffness, enabling fine-tuning for biological model engineering. Our approach allows the from-scratch fabrication of approximately 5 scaffolds in 10 min, including bioink loading, printing, and washing. Although conceived in an epithelial-only configuration, our system supports BM deposition and long-term epithelial cell maturation, but it lacks stromal, immune, vascular and neural compartments known to regulate niche homeostasis.

A key next step will be the incorporation of primary corneal stromal fibroblasts directly into the bioink prior to DLP printing. We have previously demonstrated high cell viability following photocrosslinking using the same technology [13,14], lending support to the feasibility of this approach. The main technical challenges associated with this development will include preserving stromal cell viability and phenotypic stability post-printing, particularly given the differential mechanical environments generated by the high and low UV-exposed regions of the scaffold. Additionally, scaffold transparency and structural integrity will need to be evaluated following stromal cell encapsulation. Finally, it will be essential to verify that the shape-morphing process is preserved in cell-laden constructs. Beyond corneal applications, our bioprinting approach based on shape-morphing hydrogels, where spatially programmed crosslinking densities are exploited to induce secondary conformational transitions, applies broadly to other models where shape and topography are closely intertwined to tissue function [53,54]. We believe that our single-step workflow bridges tissue-engineered complexity with practical accessibility.

5. Conclusions

This work establishes a simple, single-step Digital Light Processing platform to fabricate undulating 3D hydrogel scaffolds. It recapitulates some of the architectural features of the limbal niche and supports long-term organization of primary human limbal-derived corneal epithelial cells. By combining methacrylated collagen, hyaluronic acid, and silk fibroin into a photocurable bioink, and exploiting grayscale UV projection to generate heterogeneous crosslinking densities that induce temperature-dependent shape morphing, the system generates stable grooves and ridges within a single fabrication step. These scaffolds sustain epithelial adhesion, stratification, and apicobasal organization

for up to three weeks. Mechanotransduction analysis revealed differential YAP nuclear localization at confluency between areas exposed to different UV doses, consistent with mechanosensing described in the cornea. After prolonged culture, we observed basal enrichment of P63-positive progenitors, apical localization of PAX6-positive differentiated cells, progressive tight junction formation, and basement membrane deposition.

Beyond demonstrating proof-of-concept for a scalable, accessible technology to fabricate complex 3D scaffolds based on shape-morphing hydrogels, this study establishes the biological relevance of this approach for advanced epithelial tissue modeling. The platform's versatility extends beyond corneal applications: the ability to create spatially defined topographies through programmable UV patterns positions this approach as a broadly applicable tool for engineering complex curved biological systems [55], such as epithelial niches in microphysiological systems and/or organoid-on-chip platforms where architectural complexity is essential. Furthermore, this system offers substantial room for optimization, including systematic tuning of grayscale patterns (including continuous grayscale gradients), hydrogel thickness, and bioink composition to expand the range of achievable topographies and to establish design rules for this methodology. Together, these findings provide a technological foundation for rapid, reproducible fabrication of biomimetic scaffolds that bridge tissue-engineered complexity with practical accessibility for advanced *in vitro* modeling in basic science [56], disease modeling, drug screening, and regenerative medicine.

Data availability

The data that supports the findings of this study is available on request from the corresponding author.

CRediT authorship contribution statement

Ioannis Paschalidis: Writing – review & editing, Writing – original draft, Methodology, Investigation, Formal analysis, Data curation, Conceptualization. **François Chatelain:** Methodology, Investigation. **Remy Agniel:** Methodology, Investigation. **Christophe Sandt:** Data curation, Formal analysis, Investigation, Methodology, Writing – review & editing. **Damien Guindolet:** Methodology. **Sabrina Kellouche:** Methodology, Investigation. **Alexandra Fuchs:** Writing – original draft, Supervision, Resources, Project administration, Funding acquisition, Conceptualization. **Benoit Souquet:** Writing – review & editing, Writing – original draft, Visualization, Validation, Supervision, Resources, Project administration, Methodology, Investigation, Funding acquisition, Formal analysis, Data curation, Conceptualization. **Eric Ernest Gabison:** Writing – review & editing, Writing – original draft, Supervision, Resources, Project administration, Funding acquisition, Conceptualization.

Declaration of competing interest

The authors declare that they have no known competing financial interests or personal relationships that could have appeared to influence the work reported in this paper.

Acknowledgments

This work was funded by the internal CEA Organoids On a Chip (OOC) FOCUS incentive program. This work was supported by the French government, through the French National Research Agency (ANR), under the France 2030 program PEPR BBTI, grant ANR-24-PEBI-0001. The authors would like to thank the Conseil regional Île de France for funding the CERASEM project (grant:15013107) that has allowed the acquisition of the ZEISS Gemini SEM 300 of the Microscopie&Analyses Imaging Core Facility (I-Mat, FD4122, CY Cergy Paris University). We thank Lousineh Arakelian (Team11 IRSL U1342) for assistance in the culture of non-corneal epithelial cells. We would also like to thank the Organ procurement coordination team (Dr Stephane Welschbillig, Lydia Moursy, Sophie Vo Thanh, Clément Maling, Sophie Giraud, Claire Lefur, Nathalie Versace) for isolating the primary limbal-derived corneal epithelial cells.

Supplementary materials

Supplementary material associated with this article can be found, in the online version, at doi:10.1016/j.actbio.2026.06.002.

References

[1] J. Laurent, G. Blin, F. Chatelain, V. Vanneaux, A. Fuchs, J. Larghero, M. Théry, Convergence of microengineering and cellular self-organization towards functional tissue manufacturing, Nat. Biomed. Eng. 1 (2017) 939–956, https://doi.org/10.1038/s41551-017-0166-x.

[2] L. Moroni, J.A. Burdick, C. Highley, S.J. Lee, Y. Morimoto, S. Takeuchi, J.J. Yoo, Biofabrication strategies for 3D in vitro models and regenerative medicine, Nat. Rev. Mater. 3 (2018) 21–37, https://doi.org/10.1038/s41578-018-0006-y.

[3] C.M. Leung, P. de Haan, K. Ronaldson-Bouchard, G.-A. Kim, J. Ko, H.S. Rho, Z. Chen, P. Habibovic, N.L. Jeon, S. Takayama, M.L. Shuler, G. Vunjak-Novakovic, O. Frey, E. Verpoorte, Y.-C. Toh, A guide to the organ-on-a-chip, Nat. Rev. Methods Primer 2 (2022) 1–29, https://doi.org/10.1038/s43586-022-00118-6.

[4] L. Latta, F.C. Figueiredo, R. Ashery-Padan, J.M. Collinson, J. Daniels, S. Ferrari, N. Szentmáry, S. Solá, R. Shalom-Feuerstein, M. Lako, S. Xapelli, D. Aberdam, N. Lagali, Pathophysiology of aniridia-associated keratopathy: developmental aspects and unanswered questions, Ocul. Surf. 22 (2021) 245–266, https://doi.org/10.1016/j.jtos.2021.09.001.

[5] A. Isaacson, S. Swioklo, C.J. Connon, 3D bioprinting of a corneal stroma equivalent, Exp. Eye Res. 173 (2018) 188–193, https://doi.org/10.1016/j.exer.2018.05.010.

[6] Y. Xu, J. Liu, W. Song, Q. Wang, X. Sun, Q. Zhao, Y. Huang, H. Li, Y. Peng, J. Yuan, B. Ji, L. Ren, Biomimetic convex implant for corneal regeneration through 3D printing, Adv. Sci. 10 (2023) 2205878, https://doi.org/10.1002/advs.202205878.

[7] A. Ghosh, J. Adhikari, S. Ghosh, A.K. Bera, L. Zeenat, A.D. Rajora, V. Singh, S. Basu, F. Pati, 4D Bioprinting of self-morphed corneal equivalents using smart hybrid hydrogels, Adv. Healthc. Mater. 15 (2026) e02721, https://doi.org/10.1002/adhm.202502721.

[8] Í. Ortega, P. Deshpande, A.A. Gill, S. MacNeil, F. Claeyssens, Development of a microfabricated artificial limbus with micropockets for cell delivery to the cornea, Biofabrication 5 (2013) 025008, https://doi.org/10.1088/1758-5082/5/2/025008.

[9] H.J. Levis, I. Massie, M.A. Dziasko, A. Kaasi, J.T. Daniels, Rapid tissue engineering of biomimetic human corneal limbal crypts with 3D niche architecture, Biomaterials 34 (2013) 8860–8868, https://doi.org/10.1016/j.biomaterials.2013.08.002.

[10] E. Prina, M.H. Amer, L. Sidney, M. Tromayer, J. Moore, R. Liska, M. Bertolin, S. Ferrari, A. Hopkinson, H. Dua, J. Yang, R. Wildman, F.R.A.J. Rose, Bioinspired precision engineering of three-dimensional epithelial stem cell microniches, Adv. Biosyst. 4 (2020) 2000016, https://doi.org/10.1002/adbi.202000016.

[11] M. Kauppila, A. Mörö, J.J. Valle-Delgado, T. Ihalainen, L. Sukki, P. Puistola, P. Kallio, T. Ilmarinen, M. Österberg, H. Skottman, Towards corneal limbus In vitro model: regulation of hpsc-lscs phenotype by matrix stiffness and topography during cell differentiation process, Adv. Healthc. Mater. 12 (2023) 2301396, https://doi.org/10.1002/adhm.202301396.

[12] H.S. Dua, A. Azuara-Blanco, Limbal stem cells of the corneal epithelium, Surv. Ophthalmol. 44 (2000) 415–425, https://doi.org/10.1016/s0039-6257(00)00109-0.

[13] E. Mazari-Arrighi, D. Ayollo, W. Farhat, A. Marret, E. Gontran, P. Dupuis-Williams, J. Larghero, F. Chatelain, A. Fuchs, Construction of functional biliary epithelial branched networks with predefined geometry using digital light stereolithography, Biomaterials 279 (2021) 121207, https://doi.org/10.1016/j.biomaterials.2021.121207.

[14] E. Mazari-Arrighi, M. Lépine, D. Ayollo, L. Faivre, J. Larghero, F. Chatelain, A. Fuchs, Self-organization of long-lasting Human endothelial capillary-like networks guided by DLP bioprinting, Adv. Healthc. Mater. 13 (2024) 2302830, https://doi.org/10.1002/adhm.202302830.

[15] S. Bhattacharya, A. Mukherjee, S. Pisano, S. Dimri, E. Knaane, A. Altshuler, W. Nasser, S. Dey, L. Shi, I. Mizrahi, N. Blum, O. Jokel, A. Amitai-Lange, A. Kaganovsky, M. Mimouni, S. Socea, M. Midlij, B. Tiosano, P. Hasson, C. Feral, H. Wolfenson, R. Shalom-Feuerstein, The biophysical property of the limbal niche maintains stemness through YAP, Cell Death Differ 30 (2023) 1601–1614, https://doi.org/10.1038/s41418-023-01156-7.

[16] P.-O. Strale, A. Azioune, G. Bugnicourt, Y. Lecomte, M. Chahid, V. Studer, Multiprotein printing by light-induced molecular adsorption, Adv. Mater. 28 (2016) 2024–2029, https://doi.org/10.1002/adma.201504154.

[17] D. Guindolet, A.M. Woodward, E.E. Gabison, P. Argüeso, Glycogene expression profile of Human limbal epithelial cells with distinct clonogenic potential, Cells 11 (2022) 1575, https://doi.org/10.3390/cells11091575.

[18] N.R. Korpole, P. Kurada, M.R. Korpole, Gender difference in ocular diseases, risk factors and management with specific reference to role of sex steroid hormones, J. - Life Health 13 (2022) 20–25, https://doi.org/10.4103/jmh.jmh_28_22.
[19] J.K. Sahoo, O. Hasturk, T. Falcucci, D.L. Kaplan, Silk chemistry and biomedical material designs, Nat. Rev. Chem. 7 (2023) 302–318, https://doi.org/10.1038/s41570-023-00486-x.
[20] J. Liu, B.D. Lawrence, A. Liu, I.R. Schwab, L.A. Oliveira, M.I. Rosenblatt, Silk fibroin as a biomaterial substrate for corneal epithelial cell sheet generation, invest. Ophthalmol, Vis. Sci. 53 (2012) 4130, https://doi.org/10.1167/iovs.12-9876.
[21] S. Dupont, L. Morsut, M. Aragona, E. Enzo, S. Giulitti, M. Cordenonsi, F. Zanconato, J.L. Digabel, M. Forcato, S. Bicciato, N. Elvassore, S. Piccolo, Role of YAP/TAZ in mechanotransduction, Nature 474 (2011) 179–183, https://doi.org/10.1038/nature10137.
[22] S.M. Thomasy, B.C. Leonard, M.A. Greiner, J.M. Skeie, V.K. Raghunathan, Squishy matters – Corneal mechanobiology in health and disease, Prog. Retin. Eye Res. 99 (2024) 101234, https://doi.org/10.1016/j.preteyeres.2023.101234.
[23] A.J. Shortt, G.A. Secker, P.M. Munro, P.T. Khaw, S.J. Tuft, J.T. Daniels, Characterization of the limbal epithelial stem cell niche: novel imaging techniques permit In vivo observation and targeted biopsy of limbal epithelial stem cells, Stem Cells 25 (2007) 1402–1409, https://doi.org/10.1634/stemcells.2006-0580.
[24] P. Arpitha, N.V. Prajna, M. Srinivasan, V. Muthukkaruppan, High expression of p63 combined with a large N/C ratio defines a subset of Human limbal epithelial cells: implications on epithelial stem cells, Invest. Ophthalmol. Vis. Sci. 46 (2005) 3631, https://doi.org/10.1167/iovs.05-0343.
[25] K. Kitazawa, T. Hikichi, T. Nakamura, C. Sotozono, S. Kinoshita, S. Masui, PAX6 regulates human corneal epithelium cell identity, Exp. Eye Res. 154 (2017) 30–38, https://doi.org/10.1016/j.exer.2016.11.005.
[26] L. Wiley, N. SundarRaj, T.T. Sun, R.A. Thoft, Regional heterogeneity in human corneal and limbal epithelia: an immunohistochemical evaluation, Invest. Ophthalmol. Vis. Sci. 32 (1991) 594–602.
[27] S. Merjava, A. Neuwirth, M. Tanzerova, K. Jirsova, The spectrum of cytokeratins expressed in the adult human cornea, limbus and perilimbal conjunctiva, Histol. Histopathol. 26 (2011). https://digitum.um.es/digitum/handle/10201/48278 (accessed August 15, 2024).
[28] L.W. Chen, Y.-M. Chen, C.-J. Lu, M.-Y. Chen, S.-Y. Lin, F.-R. Hu, W.-L. Chen, Effect of air-lifting on the stemness, junctional protein formation, and cytokeratin expression of in vitro cultivated limbal epithelial cell sheets, Taiwan J. Ophthalmol. 7 (2017) 205, https://doi.org/10.4103/tjo.tjo_101_17.
[29] J.M. Wolosin, X. Xiong, M. Schütte, Z. Stegman, A. Tieng, Stem cells and differentiation stages in the limbo-corneal epithelium, Prog. Retin. Eye Res. 19 (2000) 223–255, https://doi.org/10.1016/S1350-9462(99)00005-1.
[30] A. Kirillova, R. Maxson, G. Stoychev, C.T. Gomillion, L. Ionov, 4D biofabrication using shape-morphing hydrogels, Adv. Mater. 29 (2017) 1703443, https://doi.org/10.1002/adma.201703443.
[31] S.H. Kim, Y.B. Seo, Y.K. Yeon, Y.J. Lee, H.S. Park, M.T. Sultan, J.M. Lee, J.S. Lee, O. J. Lee, H. Hong, H. Lee, O. Ajiteru, Y.J. Suh, S.-H. Song, K.-H. Lee, C.H. Park, 4D-bioprinted silk hydrogels for tissue engineering, Biomaterials 260 (2020) 120281, https://doi.org/10.1016/j.biomaterials.2020.120281.
[32] A. Matsumoto, J. Chen, A.L. Collette, U.-J. Kim, G.H. Altman, P. Cebe, D.L. Kaplan, Mechanisms of silk fibroin sol−gel transitions, J. Phys. Chem. B 110 (2006) 21630–21638, https://doi.org/10.1021/jp056350v.
[33] A. Reizabal, C.M. Costa, L. Pérez-Álvarez, J.L. Vilas-Vilela, S. Lanceros-Méndez, Silk fibroin as sustainable advanced material: material properties and characteristics, processing, and applications, Adv. Funct. Mater. 33 (2023) 2210764, https://doi.org/10.1002/adfm.202210764.
[34] M.D. Goodner, C.N. Bowman, Development of a comprehensive free radical photopolymerization model incorporating heat and mass transfer effects in thick films, Chem. Eng. Sci. 57 (2002) 887–900, https://doi.org/10.1016/S0009-2509(01)00287-1.
[35] N. Johari, L. Moroni, A. Samadikuchaksaraei, Tuning the conformation and mechanical properties of silk fibroin hydrogels, Eur. Polym. J. 134 (2020) 109842, https://doi.org/10.1016/j.eurpolymj.2020.109842.
[36] B. Tavsanli, O. Okay, Mechanically robust and stretchable silk/hyaluronic acid hydrogels, Carbohydr. Polym. 208 (2019) 413–420, https://doi.org/10.1016/j.carbpol.2018.12.088.
[37] N. Garcia-Porta, P. Fernandes, A. Queiros, J. Salgado-Borges, M. Parafita-Mato, J. M. González-Méijome, Corneal biomechanical properties in different ocular conditions and new measurement techniques, Int. Sch. Res. Not. 2014 (2014) 1–19, https://doi.org/10.1155/2014/724546.
[38] D.C. Pye, A clinical method for estimating the modulus of elasticity of the human cornea in vivo, PLoS ONE 15 (2020) e0224824, https://doi.org/10.1371/journal.pone.0224824.
[39] P. Eberwein, J. Nohava, G. Schlunck, M. Swain, Nanoindentation derived mechanical properties of the corneascleral rim of the Human eye, Biophys. J. 106 (2014) 789a, https://doi.org/10.1016/j.bpj.2013.11.4324.
[40] T. Manoochehrabadi, A. Solouki, J. Majidi, S. Khosravimelal, E. Lotfi, K. Lin, S.-H. Daryabari, M. Gholipourmalekabadi, Silk biomaterials for corneal tissue engineering: from research approaches to therapeutic potentials; a review, Int. J. Biol. Macromol. 305 (2025) 141039, https://doi.org/10.1016/j.ijbiomac.2025.141039.
[41] A.I. Teixeira, G.A. Abrams, P.J. Bertics, C.J. Murphy, P.F. Nealey, Epithelial contact guidance on well-defined micro- and nanostructured substrates, J. Cell Sci. 116 (2003) 1881–1892, https://doi.org/10.1242/jcs.00383.
[42] T.B. McKay, A.E.K. Hutcheon, X. Guo, J.D. Zieske, D. Karamichos, Modeling the cornea in 3-dimensions: current and future perspectives, Exp. Eye Res. 197 (2020) 108127, https://doi.org/10.1016/j.exer.2020.108127.
[43] J.A. Brassard, M.P. Lutolf, Engineering stem cell self-organization to build better organoids, Cell Stem Cell 24 (2019) 860–876, https://doi.org/10.1016/j.stem.2019.05.005.
[44] N. Gjorevski, M. Nikolaev, T.E. Brown, O. Mitrofanova, N. Brandenberg, F. W. DelRio, F.M. Yavitt, P. Liberali, K.S. Anseth, M.P. Lutolf, Tissue geometry drives deterministic organoid patterning, Science 375 (2022) eaaw9021, https://doi.org/10.1126/science.aaw9021.
[45] N. Koushki, A. Ghagre, L.K. Srivastava, C. Molter, A.J. Ehrlicher, Nuclear compression regulates YAP spatiotemporal fluctuations in living cells, Proc. Natl. Acad. Sci. 120 (2023) e2301285120, https://doi.org/10.1073/pnas.2301285120.
[46] J.W. Foster, R.R. Jones, C.A. Bippes, R.M. Gouveia, C.J. Connon, Differential nuclear expression of Yap in basal epithelial cells across the cornea and substrates of differing stiffness, Exp. Eye Res. 127 (2014) 37–41, https://doi.org/10.1016/j.exer.2014.06.020.
[47] R.M. Gouveia, F. Vajda, J.A. Wibowo, F. Figueiredo, C.J. Connon, YAP, ΔNp63, and β-catenin signaling pathways are involved in the modulation of corneal epithelial stem cell phenotype induced by substrate stiffness, Cells 8 (2019) 347, https://doi.org/10.3390/cells8040347.
[48] R.M. Gouveia, G. Lepert, S. Gupta, R.R. Mohan, C. Paterson, C.J. Connon, Assessment of corneal substrate biomechanics and its effect on epithelial stem cell maintenance and differentiation, Nat. Commun. 10 (2019), https://doi.org/10.1038/s41467-019-09331-6.
[49] U. Schlötzer-Schrehardt, F.E. Kruse, Identification and characterization of limbal stem cells, Exp. Eye Res. 81 (2005) 247–264, https://doi.org/10.1016/j.exer.2005.02.016.
[50] Z. Chen, C.S. de Paiva, L. Luo, F.L. Kretzer, S.C. Pflugfelder, D. Li, Characterization of putative stem cell phenotype in Human limbal epithelia, Stem Cells 22 (2004) 355–366, https://doi.org/10.1634/stemcells.22-3-355.
[51] J.D. Zieske, V.S. Mason, M.E. Wasson, S.F. Meunier, C.J.M. Nolte, N. Fukai, B. R. Olsen, N.L. Parenteau, Basement membrane assembly and differentiation of cultured corneal cells: importance of culture environment and endothelial cell interaction, Exp. Cell Res. 214 (1994) 621–633, https://doi.org/10.1006/excr.1994.1300.
[52] T.M. Shiju, L.P. Sampaio, G.S.L. Hilgert, S.E. Wilson, Corneal epithelial basement membrane assembly is mediated by epithelial cells in coordination with corneal fibroblasts during wound healing, Mol. Vis. 29 (2023) 68–86.
[53] Y. Wang, D. Stonehouse-Smith, M.T. Cobourne, J.B.A. Green, M. Seppala, Cellular mechanisms of reverse epithelial curvature in tissue morphogenesis, Front. Cell Dev. Biol. 10 (2022), https://doi.org/10.3389/fcell.2022.1066399.
[54] C. Arnold, I. Tahmaz, M.-L. Chapon, H. Maayouf, V. Luchnikov, J.-L. Milan, F. Borghi, L. Pieuchot, Bending the rules: curvature's impact on cell biology, BMC Biol. 23 (2025) 296, https://doi.org/10.1186/s12915-025-02416-3.
[55] B. Schamberger, R. Ziege, K. Anselme, M. Ben Amar, M. Bykowski, A.P.G. Castro, A. Cipitria, R.A. Coles, R. Dimova, M. Eder, S. Ehrig, L.M. Escudero, M.E. Evans, P. R. Fernandes, P. Fratzl, L. Geris, N. Gierlinger, E. Hannezo, A. Iglič, J.J. K. Kirkensgaard, P. Kollmannsberger, Ł. Kowalewska, N.A. Kurniawan, I. Papantoniou, L. Pieuchot, T.H.V. Pires, L.D. Renner, A.O. Sageman-Furnas, G. E. Schröder-Turk, A. Sengupta, V.R. Sharma, A. Tagua, C. Tomba, X. Trepat, S. L. Waters, E.F. Yeo, A. Roschger, C.M. Bidan, J.W.C. Dunlop, Curvature in biological systems: its quantification, emergence, and implications across the scales, Adv. Mater. 35 (2023) 2206110, https://doi.org/10.1002/adma.202206110.
[56] M. Luciano, S. Gabriele, Designing hydrogel dimensionality to investigate mechanobiology, Soft Matter 21 (2025) 4551–4572, https://doi.org/10.1039/D4SM01458H.